Mn-Intercalated $MoSe_2$ under pressure: electronic structure and vibrational characterization of a dilute magnetic semiconductor

Shunda Chen*, Virginia L. Johnson*,[1] Bryan P. Moser,[1]
Daniel R. Williams,[1] Davide Donadio,[1] and Kristie J. Koski[1,*]

[1] *Department of Chemistry, University of California: Davis, Davis CA 95616, USA*

(Dated: April 11, 2022)

Intercalation offers a promising way to alter the physical properties of two-dimensional (2D) layered materials. Here, Raman scattering of 2D layered $MoSe_2$ intercalated with atomic manganese is investigated at ambient and high pressure up to 7 GPa. The behavior of optical phonons is studied experimentally with a diamond anvil cell, and through density functional theory calculations. Experiment and theory show excellent agreement in optical phonon behavior. Experiment shows that the previously Raman inactive A_{2u} mode is activated and enhanced with intercalation and pressure. DFT calculations reveal a shift of Fermi level into the conduction band and spin polarization in Mn_xMoSe_2 that increases at low Mn concentration and low pressure. This study elucidates how manganese, an electron-donating magnetic intercalant, alters the pressure-dependent optical phonon and electronic behavior of $MoSe_2$. Our results suggest that intercalation and pressurization of van der Waals materials allow one to obtain dilute magnetic semiconductors with controllable properties, providing a viable route for the development of new materials for spintronic applications.

INTRODUCTION

Manganese incorporation in two-dimensional layered materials has received increasing attention as it shows promise for revolutionizing advancements in spintronics [1], ferromagnetic ordering [2–5], and tunable devices [2, 5, 6]. This has inspired doping investigations which reveal a plethora of unique magnetic behaviors. Theory and experiment have shown that Mn doping can lead to ferromagnetic ordering in 2D materials [2, 4–6]. Supercritical hydrothermal methods for Mn doping intrinsic ferromagnetism in $Mn_xMo_{1-x}S_2$ [7]. A recent study of the 2D dilute magnetic semiconductor Mn-doped MoS_2 predicts that MoS_2 doped to 10-15% manganese is ferromanetic at room temperature [3]. Calculations also predict that $MnBi_2Te_4$, an intrinsic magnetic topological insulator, is an ideal platform to realize a high-temperature quantum anomalous hall insulator states [8].

In layered materials, Mn intercalation offers a unique alternative to Mn doping. Intercalation provides a chemical handle to tune electronic structure and phonon propagation without disturbing the host lattice [9–11]. Intercalation in layered materials has demonstrated an enormous realm of physical and chemical tunability in both current and historical research [9, 11–15]. Through intercalation it is possible to adjust the superconducting temperature [11, 16], enhance transparency and conductivity [17–20], and reversibly alter optoelectronic behaviors including color and photoluminescence [18, 19, 21]. Recently a chemical route was achieved to intercalate zerovalent manganese, post-growth, into 2D layered materials [9]. Intercalation offers a new avenue for experimental study of manganese incorporated two-dimensional materials beyond that of doping.

Molybdenum diselenide ($MoSe_2$) is a heavily investigated layered n-type indirect band gap semiconductor (E_g=1.1 eV) that shows a transition to a direct band gap with reduction in the number of layers [22–24]. In a recent report, spin states protected from intrinsic electron–phonon coupling were demonstrated in monolayer $MoSe_2$, reaching 100 ns lifetimes at room temperature [25]. High-pressure investigations have shown that $MoSe_2$ does not undergo any phase transitions up to 30 GPa [26]. Above 40 GPa, a possible semiconductor-metal phase transition has been identified [27, 28]. The effect of Mn intercalation on the pressure-induced metallization of $MoSe_2$ is a point of interest, as the intercalated metal may alter the metallization behavior of van der Waals systems [29]. Whether pressure favors magnetic ordering at ambient temperature is a point of interest as an analogous mechanism, MoS_2, was observed with high concentration of substitutional Mn [3]. Pressure results in greater wavefunction overlap that could lead to a stronger coupling between isolated Mn intercalant and the $MoSe_2$ semiconductor electron density, enhancing spin polarization effects. Understanding how structure and bonding in this material system change at pressure can provide crucial insight into this fundamental nature.

Here, through both experiment and first-principles calculations, we show that the intercalation of manganese into $MoSe_2$ can alter host structure and optical phonon frequencies, giving rise to new Raman modes, and altered pressure-dependent behavior. Pressure-dependent Raman scattering was investigated up to 7 GPa under hydrostatic conditions in a diamond anvil cell, giving rise to pressure induced bonds between selenium and the manganese intercalant. First-principles calculations of Raman shifts, in excellent agreement with experiments, shed light on the changes of the magnetic and vibrational properties of Mn-intercalated $MoSe_2$ as a function of pressure and of the amount of intercalated Mn. Spin-polarized band structure calculations suggest that this

material can sustain significant spin currents, making it a suitable dilute magnetic semiconductor.

METHODS

Manganese Intercalation

Molybdenum diselenide ($MoSe_2$) was prepared by deposition from powder onto fused silica substrates followed by drop-casting ethanol onto the substrate to adhere the layered materials preventing loss in solution during intercalation. $MoSe_2$ powders were on the order of 1–100 μm with many large single-crystal platelets.

Zero-valent manganese was intercalated through the decomposition of dimanganese decacarbonyl in dilute acetone under inert atmosphere [9]. The $MoSe_2$ coated substrates were placed in a 25-50 mL round bottom flask with a reflux condenser attached to a Schlenk line, evacuated, and flushed with N_2 gas. Extra-dry acetone (5 ml) was added to the flask and heated to 48°C. A 10 mM solution of the carbonyl in 5 ml of acetone was added to the flask dropwise over the course of 1.5 hr and kept at 48°C for an additional $\sim$ 1 hr. Substrates were then removed from the solution and rinsed with acetone. All chemicals were obtained from Sigma-Aldrich.

High Pressure

High pressures were generated using an Alamax Easy-Lab mini-Bragg diamond anvil cell (DAC) with Boehler anvils with 0.6 mm culets. Spring steel gaskets were pre-indented to 80-100 μm and drilled with a 250 μm hole. Ruby spheres (Alamax) were used as a pressure calibrant. In the DAC, a solution of 4:1 v/v methanol:ethanol was used as pressure transmitting fluid. Pressures up to 7 GPa were measured to avoid all phase transitions and to remain at relatively hydrostatic pressures of the pressure transmitting fluid. Single crystal platelets were identified optically.

Characterization

Raman spectra and ruby fluorescence were measured using a home-built system with a $\lambda = 532$ nm Coherent Sapphire operating with <1 mW on the sample, Leica DMi8 inverted microscope, Princeton Instruments Isoplane SC320, and Princeton Instruments Pixis CCD camera. For Raman spectroscopy, a Semrock laser-edge filter and dichroic with an edge cutoff of $\sim$38 cm^{-1} was used. Acquisition times were on the order of 5 - 15 seconds with 10 - 20 averaged spectra. All spectra were acquired using an 1800 groove/mm grating. Scanning electron microscopy (SEM) and energy dispersive X-ray spectroscopy (EDX) were acquired on 5-10 single nanoribbons or flakes with a FEI SCIOS Dual-Beam FIB/SEM using an Oxford EDX detector with 10-20 keV accelerating voltage. Transmission electron microscopy (TEM) and selected area electron diffraction (SAED) were acquired using a JEOL 2100fac operating at 200keV. X-ray diffraction (XRD) data was acquired using a Bruker D8 Advance Eco with copper k-edge (λ=1.54 Å) X-rays. Rietveld refinement was performed with GSAS to determine lattice constants [30].

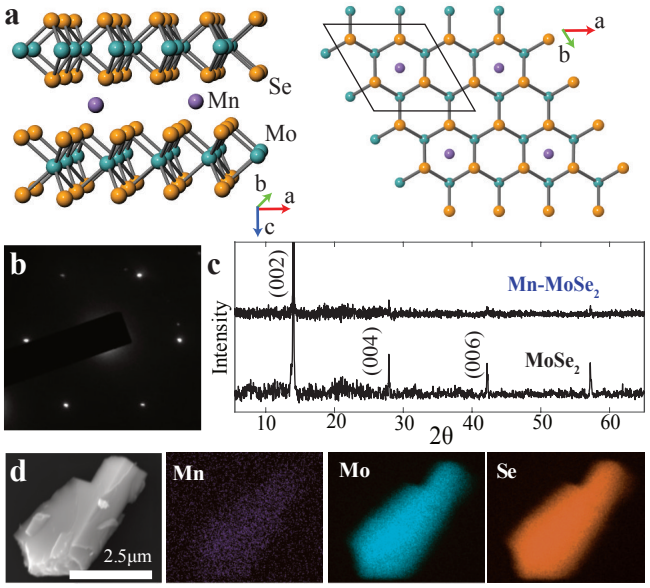

FIG. 1. (a) Hexagonal crystal structure of Mn-$MoSe_2$. Mn likely occupies octahedral sites. (b) SAED of Mn-$MoSe_2$ confirms hexagonal structure with intercalation. (c) XRD show expansion of the $MoSe_2$ host with Mn intercalation. (d) SEM-EDX of Mn-$MoSe_2$ shows Mn throughout

First-principles Calculations

Density functional theory (DFT) calculations were performed within the local density approximation (LDA) of the exchange and correlation functional [31] by using the Quantum-Espresso package [32]. Core electrons are approximated using projector augmented wave (PAW) pseudopotentials [33, 34], and the valence electronic wavefunctions are expanded in a plane-wave basis set with a kinetic energy cutoff of 49 Ry. The charge density is integrated on 16×16×4 Monkhorst-Pack meshes of k-points for pristine $MoSe_2$. Structural and cell relaxations are performed using a quasi-Newton optimization algorithm with a tight convergence criterion of 10^{-4} Ry/Bohr for maximum residual force component. To model Mn intercalation of $MoSe_2$ with different Mn concentrations of 12.5%, 6% and 3%, we used the optimized $MoSe_2$ structure to construct 2×2×1, 3×3×1, 4×4×1

supercells, and inserted a Mn atom in the vdW gap. For Mn = 25 atm %, two Mn atoms were inserted in two separate vdW gaps of a 2×2×1 supercell. We use 4×4×2 k-point mesh for 2×2×1 supercell, and 2×2×2 k-point mesh for 3×3×1 and 4×4×1 supercells. A spin-polarized framework was used to take into account the magnetic properties. The strong correlated effect of transition metal d-electrons is considered using the LDA+U method [35, 36], by introducing a Hubbard type interaction. We use a moderate U_{eff} = 4 eV for both Mo and Mn [37–41]. Other U_{eff} values, for example, 2 eV and 6 eV, were tested and consistent results were obtained. With LDA+U, the calculated band gap of pure $MoSe_2$ increases from 0.7 eV to 0.8 eV, with respect to LDA results. The frequencies of the phonon modes at the Brillouin zone center (Raman shift) as a function of pressure were calculated using density-functional perturbation theory (DFPT) [42] with optimized structures. The threshold for the iterative calculation of the perturbed Kohn-Sham wavefunctions was set to 10^{-16} Ry. This approach is well suited to predict Raman shift in monolayer and few-layer MoS_2 upon strain [43].

RESULTS AND DISCUSSION

Structure and Raman Scattering

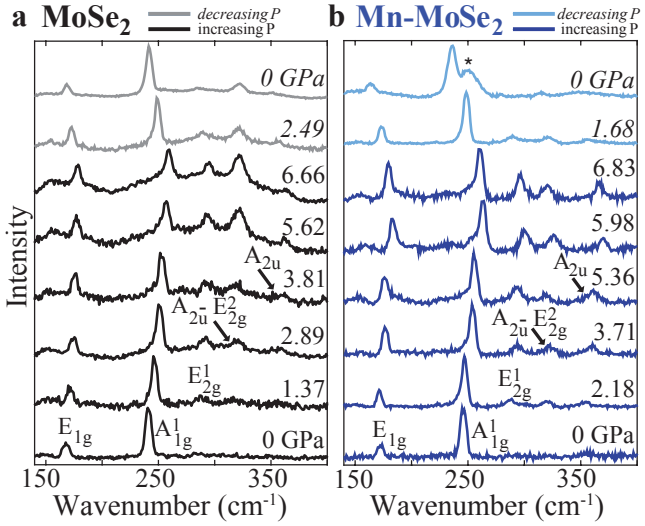

FIG. 2. (a) Raman spectra under pressure of unintercalated $MoSe_2$ and (b) Mn-intercalated $MoSe_2$. The asterisk, described in the text, coincides with the Raman frequency of a Mn-Se bond.

$MoSe_2$ has a hexagonal crystal structure (Fig. 1a; space group: $P6_3/mmc$). The host structure is maintained with intercalation as confirmed through SAED (Fig. 1b) and XRD (Fig. 1c) which show that Mn-$MoSe_2$ is hexagonal. An example SEM image with EDX elemental mapping of Mn-intercalated $MoSe_2$ (Figure 1d) show that the intercalant is distributed throughout the plates at concentrations of ∼1-2 atomic percent ($Mn_{0.02}MoSe_2$). Successful intercalation of manganese is confirmed by XRD through expansion of the host lattice constants and the unit cell volume (Table I; Fig. 1c). This expansion is associated with insertion of atoms into the van der Waals gap [9, 44]. Expansion of the unit cell volume is substantial, with an almost 3% increase even at low Mn concentrations. The volume change calculated using DFT is similar with ∼ 3-6%, depending upon the Mn intercalation concentration. Quantitatively, calculations and experiment show volume expansion of the host within the same order of ∼3% for similar intercalant concentrations. Experiment shows more expansion in the a-direction than predicted by calculation, which shows a larger increase in the c-direction associated with larger expansion of the van der Waals gap. This is likely due to

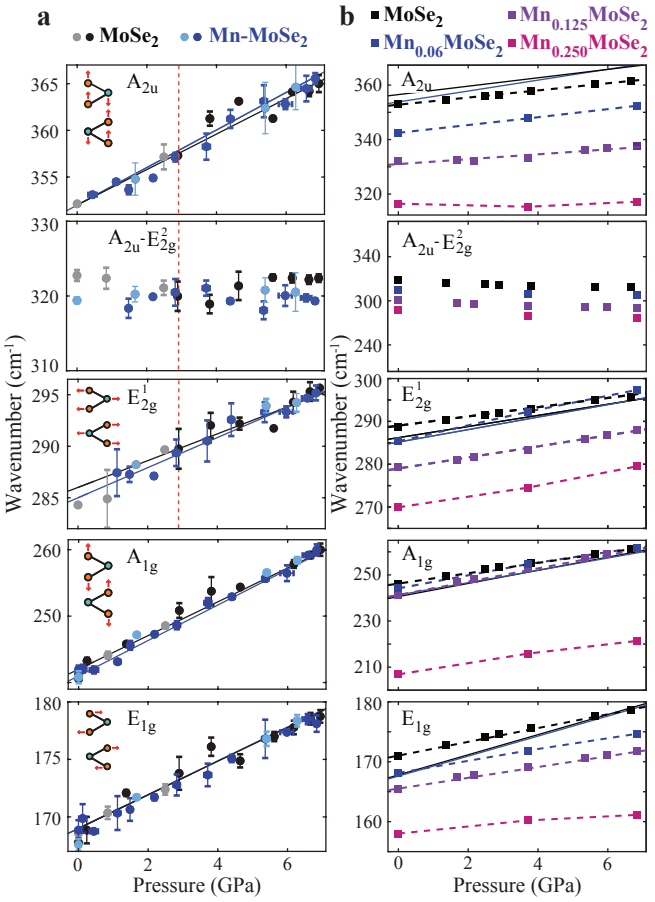

FIG. 3. (a) Experimentally determined shifts in Raman modes with pressure. Mode schematics are inset. A_{2u}, A_{2u}-E^2_{2g}, and E^1_{2g} modes appear after 2.89 GPa as indicated with a red vertical dashed line. (b) DFPT calculated Raman shifts as a function of pressure and Mn concentration show a linear increase. The linear fit of the experimental shifts are solid lines for reference.

TABLE I. Lattice constants of $MoSe_2$ and Mn-intercalated $MoSe_2$ from experiments and DFT calculations.

	a Å	c Å.	Vol. Å^3
$MoSe_2$ (Exp.)	3.285(3)	12.921(3)	120.8(2)
$MoSe_2$ (DFT)	3.260	12.718	117.0
$Mn_{0.02}MoSe_2$ (Exp.)	3.336(5)	12.940(5)	124.7(3)
$Mn_{0.03}MoSe_2$ (DFT)	3.260	12.801	117.9
$Mn_{0.06}MoSe_2$ (DFT)	3.261	12.879	118.6
$Mn_{0.125}MoSe_2$ (DFT)	3.261	13.065	120.3
$Mn_{0.25}MoSe_2$ (DFT)	3.273	13.423	124.3

larger concentrations of manganese used in calculation. These larger concentrations simplify calculations through a smaller unit cell.

Raman spectra of $MoSe_2$ and Mn-$MoSe_2$ as a function of pressure are presented in Figure 2. The observed in-plane modes are E^2_{1g} at 168 cm^{-1} and E^1_{2g} at 286 cm^{-1}. The only Raman active out-of-plane (breathing) mode is the A_{1g} mode, which is initially at 242 cm^{-1} [26]. A peak at 354 cm^{-1} is seen at pressures above 3 GPa and can be assigned as A_{2u} [22]. It is an infrared active phonon that is forbidden in Raman scattering [45], as confirmed by calculations. Previous studies observe this peak at higher excitation energies at ambient conditions and reason that resonance effects allow this peak to be observable [22, 46]. This mode has also been observed at higher pressures [27, 28]. Intercalation of manganese and application of pressure may result in symmetry breaking allowing the forbidden mode to appear in Raman spectra. Symmetry breaking may also be responsible for the appearance of the E^1_{2g} mode at higher pressures. With increasing pressure, both modes increase in scattering intensity [26–28]. Symmetry breaking with pressure is common and not unexpected. These additional peaks may have been observed in these high pressure studies over other investigations because of the high resolution grating used.

An additional feature not observed in $MoSe_2$ appears post decompression at approximately 250 cm^{-1} in Mn-$MoSe_2$ (labeled * in Fig. 2a). This peak is not found in calculations though optimization. The frequency of this mode matches a calculated longitudinal optical phonon mode in wurtzite MnSe, suggesting bonding between the Mn intercalant and the host with released pressure [47].

Figure 3 shows the measured (Fig. 3a) and calculated (Fig. 3b) vibrational frequencies for each Raman mode as a function of pressure. Inset (Fig. 3a) are diagrams of each vibrational mode. In Fig. 3b, calculated Raman shifts are plotted alongside the fit equations for the experimental data in solid black and blue line for $MoSe_2$ and Mn-$MoSe_2$, respectively. Qualitatively, at low Mn concentrations, computational and experimental results agree. Experimental concentrations of Mn intercalant were < 3 atomic %, and calculations suggest that the magnitude of the Raman shift would increase with increased Mn concentration.

Table II provides the initial Raman frequency, ω_o, and the change in frequency with pressure ($\frac{d\omega}{dP}$). These values are given for both experiment and calculation at varying concentrations. Despite a large change in the host unit cell volume (Table I), the Raman frequency shift (Table II) of the A_{1g} mode in $MoSe_2$ barely changes, and the Raman frequency shift of the in-plane mode (E^2_{1g}) increases by about one wavenumber. Though the A_{1g} mode frequency does not change significantly, the E^2_{1g} may increase slightly. However, the measurement error is comparable to the size of the shift. The Raman shift of Mn-$MoSe_2$ and $MoSe_2$ modes show nearly the same linear pressure-dependent slope ($\frac{d\omega}{dP}$) (Fig. 3,Table II). The E^1_{2g} and A_{2u} modes do not show up until pressure of ~ 1 GPa and remain with decompression [45, 48]. An anomalous mode shows up around 320 cm^{-1}. DFT calculations suggest this might be ascribed to the A_{2u}-E^2_{2g} combination band. This mode does not appear in $MoSe_2$ until almost ~ 3 GPa, as indicated by a dashed red line in Fig. 3. This mode persists with decreasing pressure, which is consistent with the appearance of the A_{2u} mode. It occurs in Mn-$MoSe_2$ at around ~ 1 GPa. This peak shows no change with pressure as Raman shifts of both the E^2_{2g} and the A_{2u} increase. Thus, there is no pressure-derivative of this mode. All modes show phonon stiffening, increasing linearly with pressure, except the overtone mode at around 320 cm^{-1} as discussed above.

Compressibility of $MoSe_2$ and $MnMoSe_2$ can be described using the isothermal mode Grüneisen parameter (γ_T):

$$\gamma_T = -\left(\frac{d\ln\omega}{d\ln V}\right)_T = \frac{B_T}{\omega_0}\left(\frac{d\omega}{dP}\right)_T \quad (1)$$

where B_T is the isothermal bulk modulus. Using the third-order Birch-Murnaghan equation of state to fit *in situ* high-pressure $MoSe_2$ X-ray diffraction data, Aksoy[49] *et al.* calculated B_T as 45.7 ± 0.3 GPa. Calculations here find a bulk modulus of 47.9 GPa for $MoSe_2$, close to experiments [49], and 51.3 GPa for $Mn_{0.125}MoSe_2$. Mn-intercalation should yield a notable decrease in the isothermal compressibility. With pressure, the empty van der Waals gap should compress first. By adding more atoms to the gap, Mn-intercalation subsumes space otherwise available for compression. Thus, intercalation makes the material less compressible. Using these values of B_T, along with the relevant values of ω_0 and $\frac{d\omega}{dP}$, the mode Grüneisen is calculated from Equation 1 for all modes (Table II).

TABLE II. Ambient pressure Raman frequencies (cm^{-1}), Raman shift pressure-derivative, $\frac{d\omega}{dP}$ ($\frac{cm^{-1}}{GPa}$), and isothermal mode Grüneisen (γ_T) for observed modes calculated from Equation (1).

	$\mathbf{E}_{1g}$			$\mathbf{A}^1_{1g}$		
	ω_o (cm^{-1})	$\frac{d\omega}{dP}\left(\frac{cm^{-1}}{GPa}\right)$	γ_T	ω_o (cm^{-1})	$\frac{d\omega}{dP}\left(\frac{cm^{-1}}{GPa}\right)$	γ_T
$MoSe_2$ (Exp.)	167.8(6)	1.68(8)	0.46(2)	240.6(6)	2.9(1)	0.54(2)
$MoSe_2$ (DFPT)	171.02	1.15(2)	0.307(5)	246.24	2.24(4)	0.416(7)
$Mn_{0.02}MoSe_2$ (Exp.)	167.6(6)	1.67(6)	0.46(2)	241.3(6)	2.67(4)	0.506(8)
$Mn_{0.06}MoSe_2$ (DFPT)	168.20	0.96(7)	0.261(2)	244.44	2.6(4)	0.486(3)
$Mn_{0.125}MoSe_2$ (DFPT)	165.52	0.90(3)	0.248(8)	241.45	1.88(5)	0.55(1)
$Mn_{0.250}MoSe_2$ (DFPT)	158.16	0.5(2)	0.144(1)	207.21	2.1(2)	0.463(3)
	$\mathbf{E}^1_{2g}$			$\mathbf{A}_{2u}$		
	ω_o (cm^{-1})	$\frac{d\omega}{dP}\left(\frac{cm^{-1}}{GPa}\right)$	γ_T	ω_o (cm^{-1})	$\frac{d\omega}{dP}\left(\frac{cm^{-1}}{GPa}\right)$	γ_T
$MoSe_2$ (Exp.)	286(1)	1.3(2)	0.21(3)	354.2(2)	1.5(4)	0.20(5)
$MoSe_2$ (DFPT)	289	1.08	0.171(1)	352.8	1.31	0.215(1)
$Mn_{0.02}MoSe_2$ (Exp.)	285.2(5)	1.5(1)	0.23(2)	351.5(5)	2.0(1)	0.26(1)
$Mn_{0.06}MoSe_2$ (DFPT)	285.48	1.8(1)	0.288(2)	342.45	1.45(3)	0.194(1)
$Mn_{0.125}MoSe_2$ (DFPT)	279	1.29	0.240(2)	331	0.899	0.1200(8)
$Mn_{0.250}MoSe_2$ (DFPT)	269.76	1.4(2)	0.237(2)	316.01	0.1(4)	0.0145(1)

Electronic Band Structure

Figure 4 shows the electronic band structures of pristine $MoSe_2$, $Mn_{0.03}MoSe_2$ and $Mn_{0.125}MoSe_2$ at 0 GPa and $\sim$ 7 GPa. For pure $MoSe_2$, with the increase of pressure, the band gap narrows from 0.8 eV at 0 GPa to 0.4 eV at 6.66 GPa (Fig. 4d). Upon intercalation of Mn, the overall host structure is retained (Fig. 4b and c).

At higher concentrations of Mn intercalant ($Mn_{0.125}MoSe_2$, Fig. 4c) the Fermi level lies deeper in the conduction band. While pressure tends to close the gap between the valence and the conduction band also in intercalated systems, the position of the Fermi level and the carriers concentration are determined by doping and do not change significantly upon compression (Fig. 5a).

The calculated projected density of states (PDOS) are shown in Fig. 4 for pristine and Mn-intercalated $MoSe_2$ at ambient pressure and at $\sim$ 7 GPa. Mn-intercalation in $MoSe_2$ shows clear signatures of spin polarization. At low concentrations of Mn ($Mn_{0.03}MoSe_2$), there is clear separation of the density of spin-up and spin-down electrons which suggest spin polarized current is possible in Mn-intercalated $MoSe_2$. With pressure, the spin separation between the spin-up and spin-down states is reduced. At 0 GPa the overall magnetic moment of the $Mn_{0.03}MoSe_2$ and $Mn_{0.125}MoSe_2$ supercell is 5.00 μ_B. With pressure (at 6.83 GPa), the overall magnetic moments reduce slightly to 4.61 μ_B and 4.54 μ_B for $Mn_{0.03}MoSe_2$ and $Mn_{0.125}MoSe_2$, respectively.

The intercalation energy per Mn atom estimated by first-principles calculations is $\sim$2 eV/atom. The intercalation energy can be calculated following Equation 2.

$$E_{intercalation} = \frac{E_{Mn_xMoSe_2} - E_{MoSe_2} - n_a E_{Mn}}{n_a} \quad (2)$$

where $E_{Mn_xMoSe_2}$ is the total energy of a $MoSe_2$ supercell intercalated with an atomic concentration x of Mn, E_{MoSe_2} is the total energy of a pristine $MoSe_2$ supercell with the same number of formula units as the intercalated system, E_{Mn} is the energy per atom of bulk *bcc* Mn, and n_a is the number of Mn atoms intercalated. The intercalation energy per Mn atom decreases with increasing Mn concentration, from 2.39 eV/atom at 3% Mn concentration to 1.96 eV/atom at 25% Mn concentration. The trend is similar as copper and silver intercalation in MoS_2 [50].

The calculated spin up and spin down carrier concentrations increase with increasing Mn, proportional to Mn concentration, and do not shift greatly with pressure (Fig. 5a). 2D semiconductors with dilute magnetic manganese impurities should have conduction completely ruled by spin polarization [1, 3]. One would expect that with increasing manganese concentration and increasing pressure, the concentration of spin-polarized carriers would also change with competing effects due to spin overlap. The spin interaction should increase as the manganese concentration increases (Fig. 4c), thus decreasing the spin-polarized carrier concentration. As pressure is increased, one would expect a similar effect, as the spin overlap and spin interaction also increase. Calculations of the total spin-polarized carrier concentration as a function of pressure and manganese concentration (Fig. 5b) reveal that the concentration of net spin-polarized carriers depends on both pressure and Mn concentration. Small concentrations of Mn show the greatest amount of spin-polarized carriers, with 3 atomic % (close to that

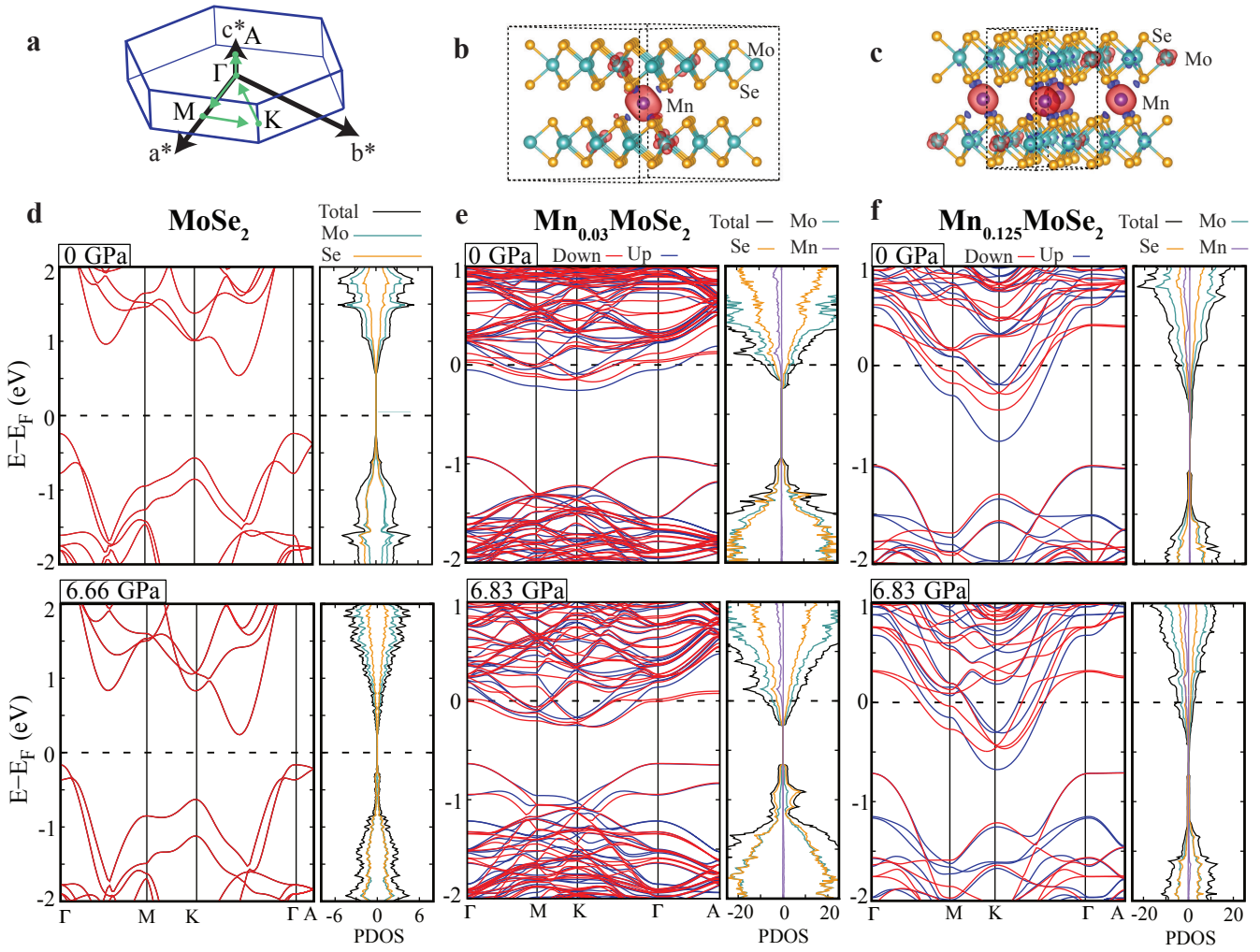

FIG. 4. (a) Brillouin zone schematic of $MoSe_2$. (b) $Mn_{0.03}MoSe_2$ structure from calculation at 0 GPa and (c) $Mn_{0.125}MoSe_2$ structure at 0 GPa with spin density and polarization; red and blue isosurfaces represent positive and negative spin density, respectively. (d) Electronic band structure of $MoSe_2$ at 0 GPa (above) and 6.66 GPa (below). Projected density of states are given for either pressure to the right of the band structure. The band structure and PDOS of (e) $Mn_{0.03}MoSe_2$ and (f) $Mn_{0.125}MoSe_2$ show that Mn intercalation metallizes the material moving the Fermi level into the conduction band. Manganese states are spin polarized in the conduction band and the population of states increases with pressure as the band gap narrows. Pressure moves the Fermi level deeper into the conduction band.

achieved by experiment) as a maximum. It is interesting that at low concentration of Mn (3%), pressure could reduce the spin-polarized carrier concentration, while at high concentration (above approximately 6%), pressure could increase the spin-polarized carrier concentration (Fig. 5b). These competing effects reveal chemical and thermodynamic tunability of $MoSe_2$ spin-polarized carriers. The predicted concentration of spin polarized carriers, up to $\sim 2 \cdot 10^{-20}$ (cm^{-3}), could be observed by Hall measurements and is significantly high to enable spintronic applications.

CONCLUSIONS

These findings set precedent for further investigation into Mn-intercalation of 2D layered materials as an alternative to dilute magnetic doping. This illustrates the ability to adjust the phonon frequencies and the electronic band structure with Mn intercalation and pressure. The robustness of this system is demonstrated by both intercalated and unintercalated pressure-dependent phonon frequencies. DFT calculations show that Mn-intercalation causes the Fermi level to shift into the conduction band, rendering the system an n-type semiconductor or nearly metallic. Manganese intercalated $MoSe_2$ retains a total magnetic moment that corresponds to that of single Mn atoms. Unpaired spins contribute to the

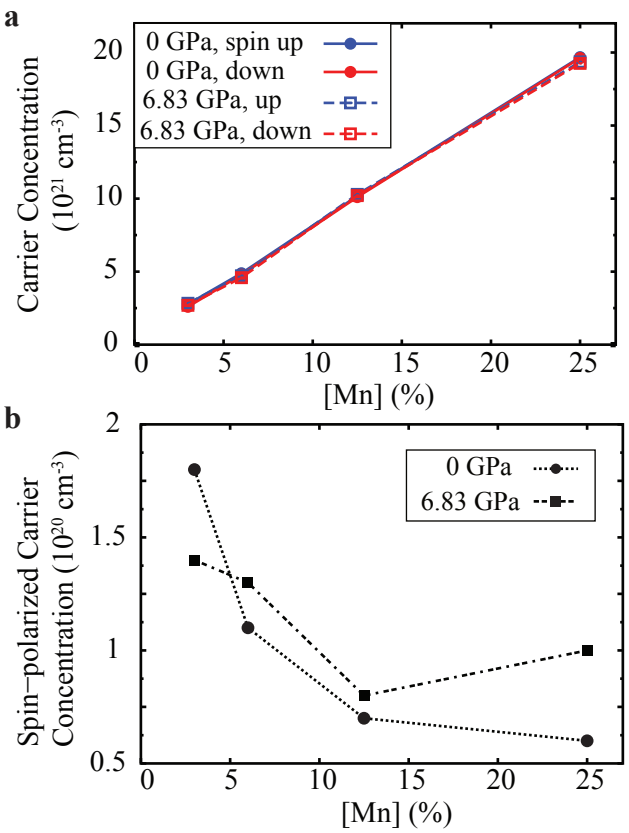

FIG. 5. (a) Spin up and spin down carrier concentration as a function of Mn concentration at 0 GPa and 6.83 GPa. (b) Total spin-polarized carrier concentration (the difference between spin up and spin down carrier concentrations).

density of states near the Fermi level, thus potentially enabling spin currents. This effect is slightly reduced with pressure at low Mn concentration, but is slightly enhanced at higher Mn concentration. The spin polarized behavior predicted in intercalated Mn-$MoSe_2$ here has the potential to surpass that of doped systems. These results provide insights into how concentration limitations in dilute manganese doped $MoSe_2$ may be bypassed by exploiting the van der Waals gap of a layered material through intercalation and pressure. We expect that resistivity studies as a function of pressure may further elucidate the nature of Mn spin-polarized carriers in this host.

ACKNOWLEDGEMENTS

This work was supported by the Office of Naval Research (N00014-16-1-3161). S.C. and V.L.J. contributed equally to this work.

REFERENCES

* koski@ucdavis.edu

[1] K. Sato, L. Bergqvist, J. Kudrnovsky, P. H. Dederichs, O. Eriksson, I. Turek, B. Sanyal, G. Bouzerar, H. Katayama-Yoshida, V. A. Dinh, T. Fukushima, H. Kizaki, and R. Zeller, Rev. Mod. Phys **82**, 1633 (2010).
[2] K. Zhang, S. Feng, J. Wang, A. Azcatl, N. Lu, R. Addou, N. Wang, C. Zhou, J. Lerach, V. Bojan, *et al.*, Nano Lett. **15**, 6586 (2015).
[3] A. Ramasubramaniam and D. Naveh, Phys. Rev. B **87**, 195201 (2013).
[4] R. Mishra, W. Zhou, S. J. Pennycook, S. T. Pantelides, and J.-C. Idrobo, Phys. Rev. B **88**, 144409 (2013).
[5] J. Wang, F. Sun, S. Yang, Y. Li, C. Zhao, M. Xu, Y. Zhang, and H. Zeng, Appl. Phys. Lett. **109**, 092401 (2016).
[6] Y. Miao, Y. Huang, H. Bao, K. Xu, F. Ma, and P. K. Chu, J. Phys. Condens. Matter **30**, 215801 (2018).
[7] H. Tan, W. Hu, C. Wang, C. Ma, H. Duan, W. Yan, L. Cai, P. Guo, Z. Sun, Q. Liu, *et al.*, Small **13**, 1701389 (2017).
[8] S. H. Lee, Y. Zhu, Y. Wang, L. Miao, T. Pillsbury, S. Kempinger, D. Graf, N. Alem, C.-Z. Chang, N. Samarth, *et al.*, arXiv:1812.00339 [cond-mat.mtrl-sci] (2018).
[9] M. Wang, D. Williams, G. Lahti, S. Teshima, D. D. Aguilar, R. Perry, and K. J. Koski, 2D Mater. **5**, 045005 (2018).
[10] M. Whittingham, Prog. Solid State Chem. **12**, 41 (1978).
[11] M. S. Dresselhaus, *Intercalation in layered materials*, Vol. 148 (Springer, 2013).
[12] W. Müller-Warmuth and R. Schöllhorn, *Progress in intercalation research*, Vol. 17 (Springer Science & Business Media, 2012).
[13] K. P. Chen, F. R. Chung, M. Wang, and K. J. Koski, J. Am. Chem. Soc. **137**, 5431 (2015).
[14] A. Sood, F. Xiong, S. Chen, H. Wang, D. Selli, J. Zhang, C. J. McClellan, J. Sun, D. Donadio, Y. Cui, E. Pop, and K. E. Goodson, Nat. Commun. **9**, 4510 (2018).
[15] S. Chen, A. Sood, E. Pop, K. E. Goodson, and D. Donadio, 2D Mater. **6**, 025033 (2019).
[16] F. Gamble, F. DiSalvo, R. Klemm, and T. Geballe, Sci. **168**, 568 (1970).
[17] M. Wang, I. Al-Dhahir, J. Appiah, and K. J. Koski, Chem. Mater. **29**, 1650 (2017).
[18] W. Bao, J. Wan, X. Han, X. Cai, H. Zhu, D. Kim, D. Ma, Y. Xu, J. N. Munday, H. D. Drew, *et al.*, Nat. Commun. **5**, 4224 (2014).
[19] Y. Gong, H. Yuan, C.-L. Wu, P. Tang, S.-Z. Yang, A. Yang, G. Li, B. Liu, J. van de Groep, M. L. Brongersma, *et al.*, Nat. Nano. **13**, 294 (2018).
[20] G. Zhu, J. Liu, Q. Zheng, R. Zhang, D. Li, D. Banerjee, and D. G. Cahill, Nat. Commun. **7**, 13211 (2016).
[21] M. Wang and K. J. Koski, ACS Nano **9**, 3226 (2015).
[22] G. Froehlicher, E. Lorchat, O. Zill, M. Romeo, and S. Berciaud, J. Raman. Spectrosc. **49**, 91 (2018).

[23] K. F. Mak, C. Lee, J. Hone, J. Shan, and T. F. Heinz, Phys. Rev. Lett. **105**, 136805 (2010).

[24] Q. H. Wang, K. Kalantar-Zadeh, A. Kis, J. N. Coleman, and M. S. Strano, Nat. Nanotech. **7**, 699 (2012).

[25] M. Ersfeld, F. Volmer, P. M. M. C. de Melo, R. de Winter, M. Heithoff, Z. Zanolli, C. Stampfer, M. J. Verstraete, and B. Beschoten, Nano Letters **19**, 4083 (2019).

[26] S. Caramazza, F. Capitani, C. Marini, A. Mancini, L. Malavasi, P. Dore, and P. Postorino, in *J. Phys. Conf. Ser*, Vol. 950 (IOP Publishing, 2017) p. 042012.

[27] L. Yang, L. Dai, H. Li, H. Hu, K. Liu, C. Pu, M. Hong, and P. Liu, RSC Advances **9**, 5794 (2019).

[28] Z. Zhao, H. Zhang, H. Yuan, S. Wang, Y. Lin, Q. Zeng, G. Xu, Z. Liu, G. Solanki, K. Patel, *et al.*, Nat Commun. **6**, 7312 (2015).

[29] V. L. Johnson, A. Anilao, and K. J. Koski, Nano Res. , 1 (2019).

[30] N. Wahlberg, N. Bindzus, L. Bjerg, J. Becker, A.-C. Dippel, and B. B. Iversen, Acta Crystallogr. A **72**, 28 (2016).

[31] J. P. Perdew and A. Zunger, Phys. Rev. B **23**, 5048 (1981).

[32] P. Giannozzi, O. Andreussi, T. Brumme, O. Bunau, M. B. Nardelli, M. Calandra, R. Car, C. Cavazzoni, D. Ceresoli, M. Cococcioni, *et al.*, J. Phys. Condens. Matter **29**, 465901 (2017).

[33] P. E. Blöchl, Phys. Rev. B **50**, 17953 (1994).

[34] G. Kresse and D. Joubert, Phys. Rev. B **59**, 1758 (1999).

[35] V. I. Anisimov, J. Zaanen, and O. K. Andersen, Phys. Rev. B **44**, 943 (1991).

[36] M. Cococcioni and S. de Gironcoli, Phys. Rev. B **71**, 035105 (2005).

[37] F. Zhou, M. Cococcioni, C. A. Marianetti, D. Morgan, and G. Ceder, Phys. Rev. B **70**, 235121 (2004).

[38] L. Wang, T. Maxisch, and G. Ceder, Phys. Rev. B **73**, 195107 (2006).

[39] A. Jain, G. Hautier, S. P. Ong, C. J. Moore, C. C. Fischer, K. A. Persson, and G. Ceder, Phys. Rev. B **84**, 045115 (2011).

[40] A. N. Andriotis and M. Menon, Phys. Rev. B **90**, 125304 (2014).

[41] M. Wu, X. Yao, Y. Hao, H. Dong, Y. Cheng, H. Liu, F. Lu, W. Wang, K. Cho, and W.-H. Wang, Phys. Lett. A **382**, 111 (2018).

[42] S. Baroni, S. de Gironcoli, A. Dal Corso, and P. Giannozzi, Rev. Mod. Phys. **73**, 515 (2001).

[43] C. Rice, R. J. Young, R. Zan, U. Bangert, D. Wolverson, T. Georgiou, R. Jalil, and K. S. Novoselov, Phys. Rev. B **87**, 081307(R) (2013).

[44] A. Powell, Annu. Rep. Prog. Chem., Sect. C: Phys. Chem. **90**, 177 (1993).

[45] O. Agnihotri, H. Sehgal, and A. Garg, Solid State Commun. **12**, 135 (1973).

[46] D. Nam, J.-U. Lee, and H. Cheong, Sci. Rep. **5**, 17113 (2015).

[47] P. D. Lao, Y. Guo, G. G. Siu, and S. C. Shen, Phys. Rev. B **48**, 11701 (1993).

[48] T. Sekine, M. Izumi, T. Nakashizu, K. Uchinokura, and E. Matsuura, J. Phys. Soc. Jpn. **49**, 1069 (1980).

[49] R. Aksoy, E. Selvi, and Y. Ma, J. Phys. Chem. Solids **69**, 2138 (2008).

[50] D. M. Guzman, N. Onofrio, and A. Strachan, J. Appl. Phys. **121**, 055703 (2017).